Failure of Cross-Rolled Beryllium Plates due to a Point Load

P.N. Roschke and E. Mascorro

Failure prediction of cross-rolled beryllium SR-200 sheets loaded in a complex state of stress was demonstrated by means of the Tsai-Wu failure theory. A total of sixteen beryllium plates, 2.54 mm thick with various length-to-width ratios and support conditions, were tested in the laboratory with a central transverse point load. Finite-element analyses of the plates were coupled with the failure prediction theory. Prediction of failure from numerical simulation was compared with strain gage and displacement transducer measurements. Analysis of the load history of the specimens revealed a primary and an ultimate failure load. Ultimate failure of a fully clamped plate caused an unusual delamination phenomenon, whereby a circular region displaced in the direction of the load, but did not separate from the plate.

Keywords

failure analysis, finite element, plate, SR-200 beryllium, strain, stress

1. Introduction

THIN beryllium sheets are known to fail in a brittle manner when deformed by out-of-plane loadings. The brittle character of beryllium sheet material that is loaded in a complex state of stress can lead to unexpected modes of failure. Prediction of such events is especially important for structures that are to be launched into space. Orbit-bound spacecraft such as the shuttle carry payloads and satellites made of beryllium that undergo a variety of static and dynamic loadings. Space flight agencies are committed to safety of the crew and machinery, and would benefit from the ability to predict loading conditions under which these structural elements can be expected to fail.

Toward this end, the Tsai-Wu failure theory (Ref 1) has been recently applied to cross-rolled SR-200 beryllium sheet (Ref 2-4). A series of laboratory experiments led to a determination of coefficients for the scalar prediction equation. The current work validated the failure criterion by experimentally testing a series of plates. The study was designed to add to the existing experimental database for beryllium sheet material, as well as to improve prediction of failure for a material that behaves in an unusual manner when loaded under a complex state of stress. (The approach taken is independent of micromechanical properties; therefore, no micrographs were taken during the investigation.)

2. Failure Theory

A general approach to failure prediction of anisotropic material has been presented by Tsai and Wu (Ref 1), who proposed the following tensor formulation to define the failure surface:

$$f(\sigma_k) = F_i\sigma_i + F_{ij}\sigma_i\sigma_j = 1 \quad \text{(Eq 1)}$$

where F_i and F_{ij} are experimentally determined constants that are unique to a given material, and σ_i is a contracted form of the second-order stress tensor σ_{ij}. For orthotropic material in plane stress, Eq 1 has the following contracted tensor form (Ref 1):

$$F_{11}\sigma_x^2 + F_{22}\sigma_y^2 + F_{66}\sigma_{xy}^2 + 2F_{12}\sigma_x\sigma_y + F_1\sigma_x + F_2\sigma_y = 1 \quad \text{(Eq 2)}$$

where σ_x, σ_y, and σ_{xy} are normal and shear stresses, respectively, that are aligned with the principal axes of the material. This formulation takes into account the interdependence of combined states of stress. The difference between positive and negative stress-induced failures is accounted for by the linear terms. Quadratic terms of the criterion describe an ellipsoid in the stress space.

Determination of principal strength coefficients F_1, F_2, F_{11}, and F_{22} of beryllium sheet requires that the ultimate uniaxial tensile and compressive stresses in the longitudinal and transverse in-plane directions be known. If the longitudinal material direction is designated as the "*1*" *axis*, F_1 and F_{11} can be determined from Eq 2:

$$F_1 = \frac{1}{\sigma_t} + \frac{1}{\sigma_c} \quad \text{(Eq 3)}$$

$$F_{11} = \frac{-1}{\sigma_t\sigma_c} \quad \text{(Eq 4)}$$

where σ_t and σ_c are ultimate tensile and compressive stresses, respectively, for a uniaxial load in the longitudinal direction (Ref 1). An interchange of subscripts in these equations leads to calculation of F_2 and F_{22} from ultimate stresses in the transverse direction. The biaxial stress coefficient, F_{12}, is computed as:

P.N. Roschke, Department of Civil Engineering, Texas A&M University, College Station, TX 77843-3136, USA; **E. Mascorro,** Mustang Engineering, Houston, TX 77084, USA.

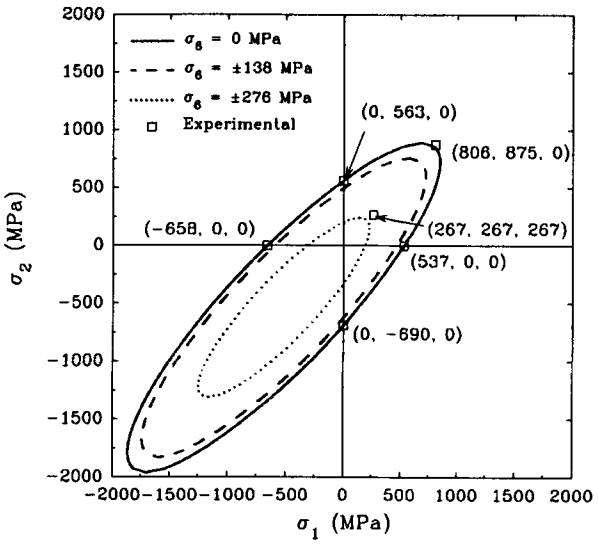

Fig. 1 Contours of failure stresses for SR-200 beryllium sheet

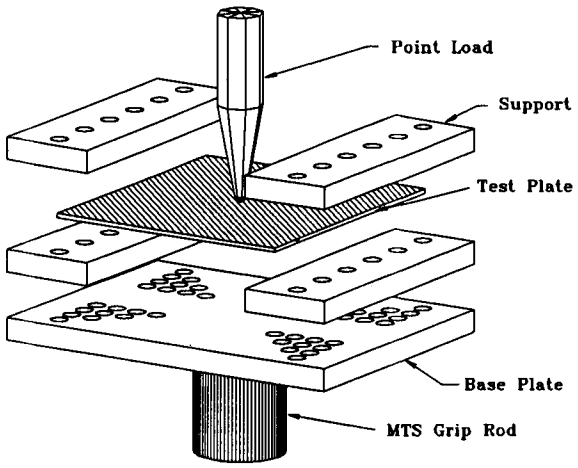

Fig. 2 Clamped-free test arrangement

Table 1 Tsai-Wu failure coefficients

Coefficient	Numerical value
F_1	3.38×10^{-10} Pa –1
F_2	3.28×10^{-10} Pa^{-1}
F_{11}	2.84×10^{-18} Pa^{-2}
F_{22}	2.57×10^{-18} Pa^{-2}
F_{66}	1.08×10^{-17} Pa^{-2}
F_{12}	-2.38×10^{-18} Pa –2

$$F_{12} = \frac{[1 - \sigma_b(F_1 + F_2) - \sigma_b^2(F_{11} + F_{22})]}{2\sigma_b^2} \quad \text{(Eq 5)}$$

where σ_b is the biaxial failure stress for $\sigma_x = \sigma_y$. The pure shear coefficient, F_{66}, is determined from:

$$F_{66} = \frac{[4 - \sigma_0(F_1 + F_2) - \sigma_0^2(F_{11} + F_{22} + 2F_{12})]}{\sigma_0^2} \quad \text{(Eq 6)}$$

where σ_0 is the failure stress obtained from an experiment in which a specimen is cut at a 45° angle from the principal material directions of a beryllium sheet (Ref 3).

As mentioned earlier, a series of laboratory experiments was carried out to determine σ_t, σ_c, σ_b, and σ_0 and, therefore, the F_i and F_{ij} coefficients for the Tsai-Wu prediction equations (Ref 3, 4). Using results of these tests in conjunction with Eq 3 to 6 led to the coefficients for SR-200 beryllium sheet shown in Table 1.

Substituting these coefficients into Eq 2 and selecting three discrete values of in-plane shearing stress produced the contours of Fig. 1, which is a two-dimensional representation of the three-dimensional failure surface. Each contour represents a failure envelope for σ_1 and σ_2 stresses corresponding to a specified value of in-plane shear stress (σ_6). The curves are nearly symmetrical about the $\sigma_1 = \sigma_2$ line. For example, if an in-plane shear stress of 276 MPa exists, then the material is predicted not to fail if the magnitudes of the σ_1 and σ_2 stresses lie inside the 276 MPa contour.

3. Experimental Method

Verification of the Tsai-Wu criterion was performed by laboratory testing of a series of beryllium plates subjected to a central concentrated load. A total of 16 plates were tested, each having a thickness of 2.54 mm and various length-to-width ratios and support conditions. As summarized in Table 2, length and width dimensions of the specimens varied from 25.4 by 25.4 mm to 101.6 by 101.6 mm in 25.4 mm increments. All specimen dimensions listed in Table 2 are from support to support. Each plate was cut from an SR-200 beryllium sheet and chemically etched 0.0076 mm on each side to remove surface flaws.

Actual dimensions for clamped-clamped plates (specimens 1 to 14) were 50.8 mm longer in the transverse direction and 38.1 mm longer in the longitudinal direction. The extra area was used to grip the plate. Each specimen was clamped on all four edges, with two exceptions: a 63.5 by 76.2 mm specimen and a 63.5 by 101.6 mm specimen were clamped on two opposite edges and were free on the remaining two edges. For the clamped-free plates (specimens 15 and 16), only the dimension in the transverse direction was 50.8 mm longer.

Boundary support conditions were achieved using a specially designed fixture. An exploded view of the method of mounting a clamped-free specimen is shown in Fig. 2. Each plate was sandwiched between four (clamped-free) or eight (clamped-clamped) steel supports that, in turn, were mounted on top of a 19.1 by 152.4 by 203.2 mm steel base plate. A point load was imposed by a steel rod with a rounded end. The rod was hardened to a 50/55 HRC rating. The tip of the rod had a semispherical end radius of 3.175 mm.

Each plate specimen was mounted in the test fixture and loaded with a universal testing machine via the loading rod (Fig. 2). Deflection of the center of each plate was measured

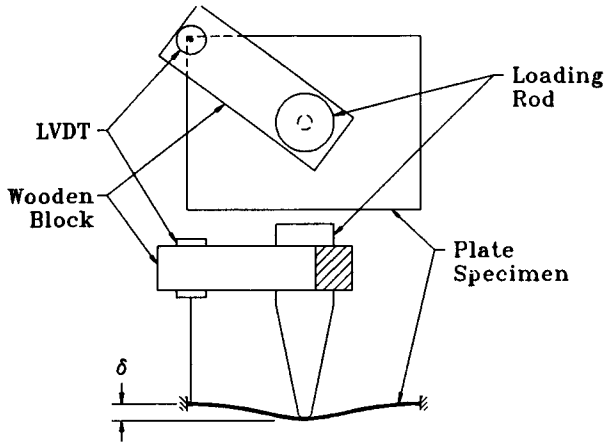

Fig. 3 Position of loading rod and LVDT

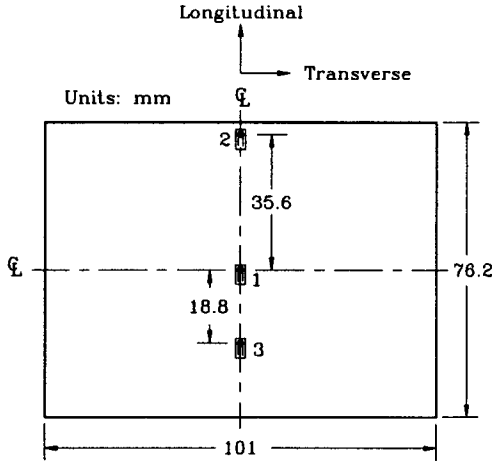

Fig. 4 Placement of strain gages for specimen 10

Table 2 Dimensions and edge conditions of plate bending specimens

Specimen No.	Thickness, mm	Longitudinal clear span, mm	Transverse clear span, mm	Edge condition
1	2.46	25.4	25.4	Clamped
2	2.54	25.4	50.8	Clamped
3	2.54	50.8	25.4	Clamped
4	2.49	50.8	50.8	Clamped
5	2.57	50.8	76.2	Clamped
6	2.57	50.8	101.6	Clamped
7	2.59	76.2	25.4	Clamped
8	2.57	76.2	50.8	Clamped
9	2.46	76.2	76.2	Clamped
10	2.59	76.2	101.6	Clamped
11	2.57	101.6	25.4	Clamped
12	2.57	101.6	50.8	Clamped
13	2.57	101.6	76.2	Clamped
14	2.49	101.6	101.6	Clamped
15	2.54	63.5	76.2	Clamped-free
16	2.57	63.5	101.6	Clamped-free

relative to one corner of the plate with the aid of a linear variable differential transformer (LVDT) with a range of ±2.54 mm (see Fig. 3). This measurement was taken as the total center deflection. The LVDT was attached to the loading rod by means of a wooden block. One end of the LVDT movable rod was positioned in one corner of the plate. Strain was measured with standard foil gages. As an example, placement of strain gages on the bottom of specimen 10 is shown in Fig. 4. Transducers from a load cell, the LVDT, and strain gages were connected to a data acquisition system. The rate of loading was approximately 8.2 N/s. All specimens were tested at a room temperature of 22 °C.

4. Results

Analysis of the load history for each specimen, with the exception of the two clamped-free specimens, revealed two incidents of load redistribution. For example, curves of load versus center deflection for specimens 4 and 9 are given in Fig. 5. Each plate exhibited a primary failure followed by an ultimate failure at a load that was approximately 50% greater than the primary failure.

4.1 *Primary Failure of Fully Clamped Specimens*

Primary failure is recognized by an audible sound, a sudden increase in displacement, and failure of the strain gage immediately beneath the concentrated load. Figures 6 and 7 show load versus deflection and load versus strain, respectively, for specimen 10 up to primary failure. For ease of comparison, results of numerical simulation are also shown. The primary failure for each fully clamped plate was due to a maximum tensile stress that occurred directly under the location of the point load. After initial failure the specimen had a number of cracks that were manifested by dye penetrant (Fig. 8). These cracks radiated from the center of the plate on the opposite side of the point of contact.

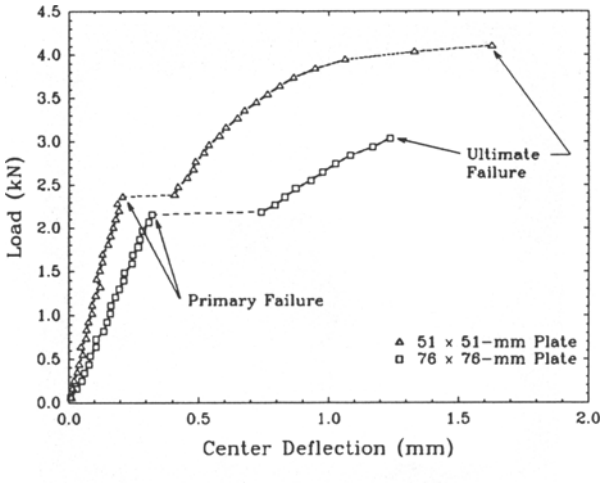

Fig. 5 Load versus center deflection for specimens 4 and 9

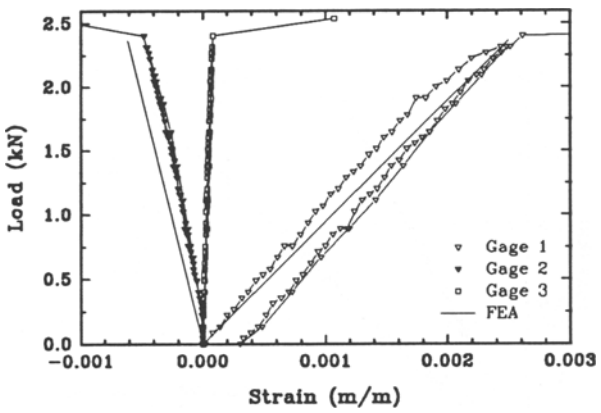

Fig. 6 Load versus center deflection for specimen 10

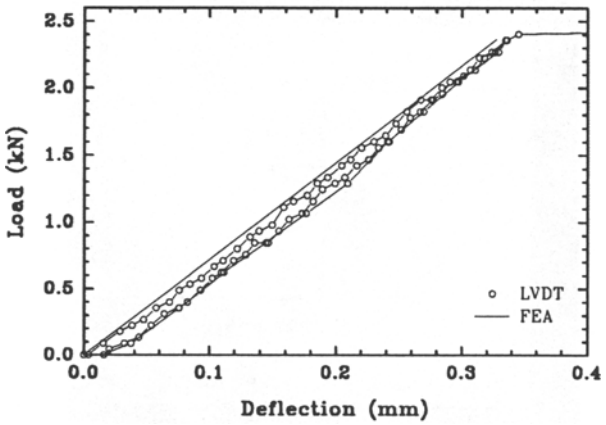

Fig. 7 Load versus normal strain for specimen 10

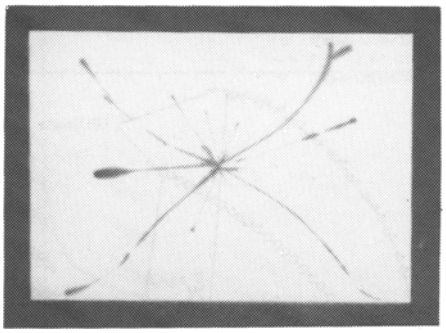

Fig. 8 Bottom of specimen 8 with dye penetrant after primary failure

Table 3 Primary and ultimate failure loads for plate specimens

Specimen No.	Primary failure load, kN	Numerical failure load, kN	Error, %	Ultimate failure load, kN
1	2.624	2.793	–6.4	...
2	2.446	2.776	–13.5	5.293
3	2.891	2.882	0.3	5.604
4	2.357	2.331	1.1	4.101
5	2.758	2.580	6.5	3.968
6	2.491	2.430	2.5	...
7	2.802	2.962	–5.7	5.382
8	2.491	2.642	–6.1	...
9	2.157	2.135	1.0	3.425
10	2.446	2.411	1.5	...
11	2.580	2.887	–11.9	4.448
12	2.535	2.522	0.5	4.848
13	2.446	2.371	0.9	...
14	2.135	2.233	–4.6	...
15	2.402	2.371	–1.3	...
16	2.402	2.148	–10.6	...

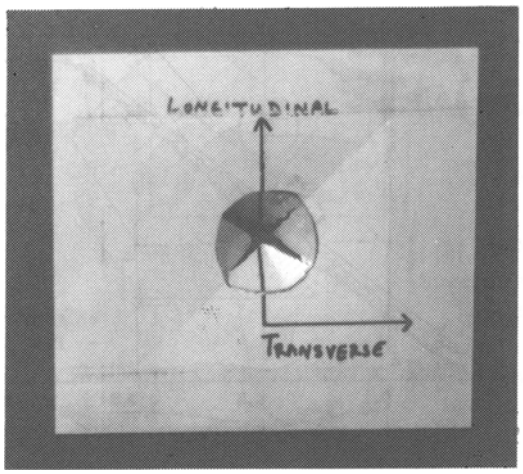

(a)

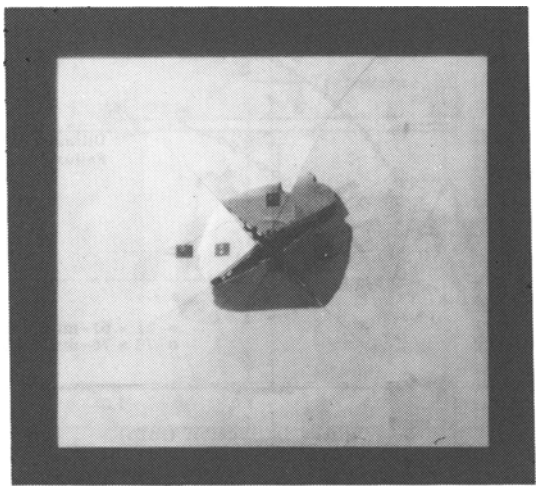

(b)

Fig. 9 Specimen 9 after ultimate failure. (a) Top. (b) Bottom.

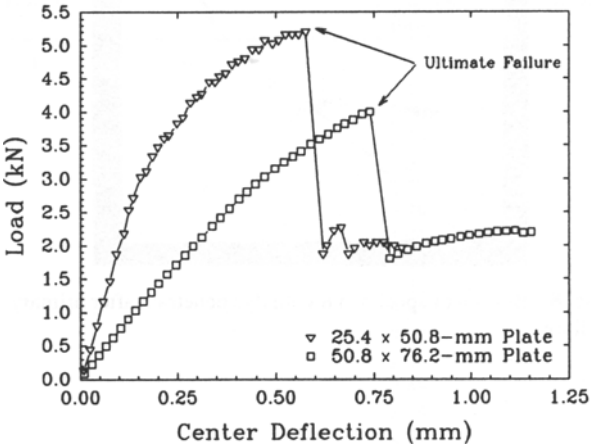

Fig. 10 Load versus center deflection for specimens 2 and 5 after primary failure

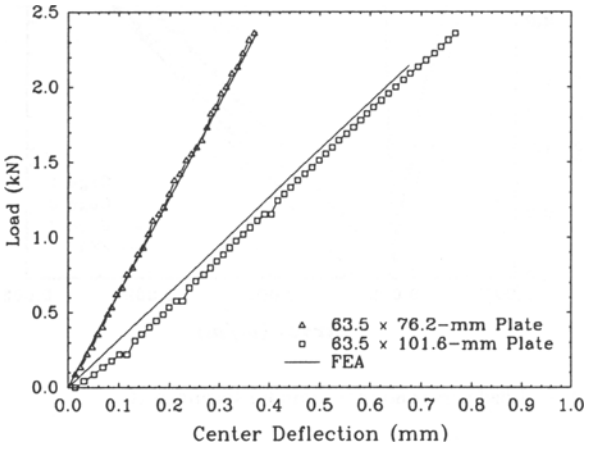

Fig. 11 Load versus center deflection for clamped-free specimens

To improve understanding of the different failure mechanisms, plates 2, 5, 6, 7, and 11 were loaded to primary failure, unloaded, and reloaded in stroke control to ultimate failure. Plates 1, 8, 10, 13, and 14 were loaded only to primary failure. Plates 3, 4, 9, 12, 15, and 16 were simply loaded to failure in load control. Table 3 summarizes primary and ultimate failure loads, where available, for each plate.

Graphs of load versus center deflection for all plates were linear up to the primary failure and showed an abrupt increase in deflection immediately afterward (Fig. 6). The load versus normal strain curves for gages not located under the point load were very nearly linear (Fig. 4 and 7). Graphs of load versus normal strain for the gage placed directly under the steel rod were nonlinear after approximately 70% of the primary failure load was reached. This nonlinearity was investigated by loading specimens 5 and 10 to a load level that was slightly below the primary failure load, unloading, and reloading (Fig. 7). The gage at the center of each plate showed residual strain. This strain was likely due to microcracking of the material or localized yielding due to the point loading on the opposite side.

4.2 *Postprimary Failure of Fully Clamped Specimens*

At ultimate failure, a nearly circular region of the material displaced in the direction of the load and fractured into a set of pie-shaped wedges (Fig. 9). The wedges, usually numbering four or five, remained partially attached to the plate along the periphery of the circular region. Also, close inspection of the specimens revealed delaminations of beryllium along the circular edge of the opening.

Specimens 2, 5, 6, 7, and 11 were loaded to primary failure and unloaded to zero. The testing machine was then switched from load to stroke control. Each plate was reloaded at a rate of 0.0085 mm/s to its ultimate load. Figure 10 shows the postpri-

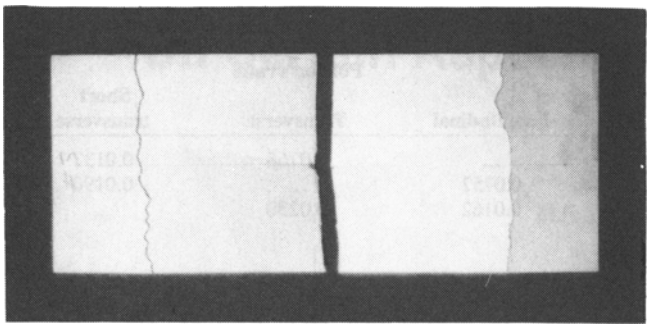

Fig. 12 Clamped-free specimen 16 after failure

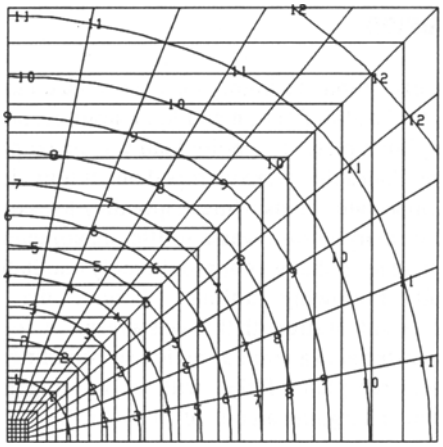

Fig. 14 Contours of vertical displacement for specimen 14

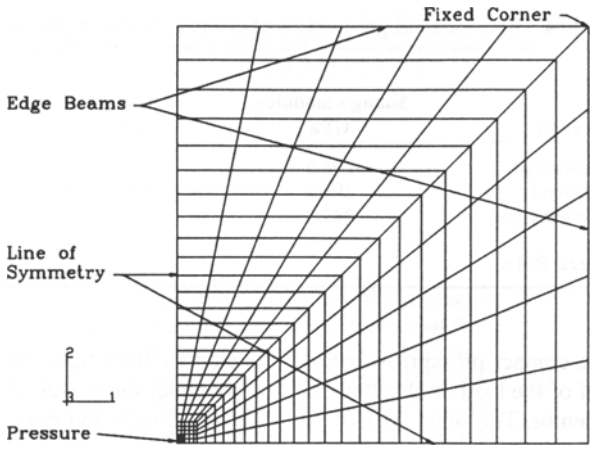

Fig. 13 Finite-element mesh for specimen 14

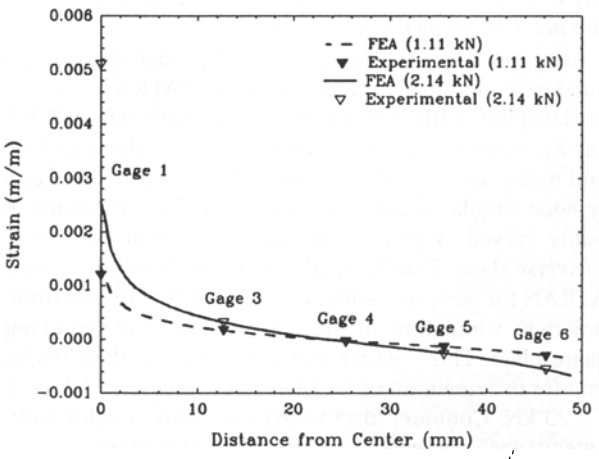

Fig. 15 Normal strain versus distance from center for specimen 14

mary failure load versus center deflection for specimens 2 and 5. After ultimate failure, each plate exhibited a residual strength of approximately 2 kN before complete penetration by the loading rod.

4.3 *Failure of Clamped-Free Specimens*

The clamped-free plates (specimens 15 and 16) were fixed along the width dimension. As indicated in Fig. 11, curves of load versus center deflection were essentially linear up to failure. Curves of load versus normal strain for the gages were similar to those obtained from fully clamped plates. Normal strain directly under the load was linear up to approximately 70% of the failure load and then became nonlinear. The relationship of the load versus strain curves for off-center gages placed on specimens 15 and 16 was entirely linear. Both of these specimens failed at a load of 2.4 kN. Unlike the totally clamped plates, there was no distinction between primary and ultimate failure; both occurred simultaneously.

After failure, both plates exhibited three distinct lines of fracture (Fig. 12). Unlike the clamped-clamped plates, no circular delamination region was evident. Parallel lines of fracture were located along the supports and at the center. Specimen 15 had a similar appearance.

5. Numerical Simulation

Loading and response of each specimen were numerically modeled using linear, elastic finite-element analysis (FEA). The geometrical model of each plate was developed with PATRAN PLUS (Ref 5). Orthotropic material properties for SR-200 sheet are listed in Table 4. Because there was geometrical and loading symmetry along two axes, only one quadrant of each plate was modeled. Theoretical clamped-edge conditions of no displacement and no rotation were not experimentally achievable. In order to accurately simulate the edge conditions applied to the plates in the laboratory, three-noded beam elements were placed along the support edges of each plate (Ref 3) (Fig. 13). Stiffness of these beam elements was adjusted so that the deflection at the center of the plate as predicted by numerical simulation matched the deflection obtained from the LVDT during the experiment.

Load was applied using a uniformly distributed pressure on the face of the four elements located under the point of loading.

Table 4 Mechanical properties of cross-rolled beryllium for tensile loading

Direction	Young's modulus, GPa	Yield stress, MPa	Failure stress, MPa	Poisson's ratio		
				Longitudinal	Transverse	Short transverse
Longitudinal	298.5	383.1	537.4	...	0.0768	0.0137
Transverse	293.4	385.8	563.6	0.0752	...	0.0190
Short transverse	347.3	...	199.8	0.0162	0.0230	...

Source: Ref 6

The contact pressure was approximated by distributing one-half of the load on the element directly under the center of the indentor. The other half of the load was distributed over the three elements adjacent to the centermost element. Total area of contact was 1.032 mm^2. The assumed distribution of pressure was from the solution of two bodies in contact, as presented by Timoshenko (Ref 7).

Clamped-free specimens 15 and 16 were modeled identically to specimens 1 to 14, except that the edge beam elements were not used along the free edges.

After the mesh geometry, material properties, loads, and boundary conditions were developed in PATRAN, they were translated into a file with a format compatible with ABAQUS (Ref 8). Approximately 250 quadratic plate elements having eight nodes, reduced integration, and five degrees of freedom per node simulated each specimen. The finite elements were doubly curved isoparametric shells that included effects of transverse shear. Finally, results of the analysis were output to PATRAN for postprocessing. Figure 14 shows results from the numerical simulation of specimen 14, a clamped-clamped square plate. This contour plot shows out-of-plane displacement for one quadrant of the plate at the predicted failure load of 2.23 kN. Contours form nearly concentric circles with the center of each circle located at the point of loading.

A graph of normal strain in the transverse material direction versus distance from the center of the plate (see Fig. 15) allowed comparison of numerical and experimental results at two levels of load for specimen 14. Excellent agreement was shown for a load that was approximately one-half of the primary failure load. Furthermore, agreement was also very good at the primary failure load for all gages, except at the center of the plate. Lack of correlation was a result of localized plastic strain or microcracking that was reported by the gage at this location but not simulated by the linear material model used in the FEA.

Predictions of stress levels were available from FEA at all integration points within the plate. For a given increment of load, the stresses in the material were substituted into Eq 2 at each integration point. If stresses at all locations in the structure rendered the left side of Eq 2 less than unity, the component was predicted not to fail. In this case the load was increased and the process repeated until the failure criterion was satisfied at at least one point in the continuum. Results of the simulation are shown in Table 3 for facile comparison with experimental values. Although deviation between some of the load magnitudes is evident, predicted failure loads are generally in good agreement with experimental failure loads.

6. Conclusion

With the exception of a highly localized area under the point of loading, the load-deflection and load-strain response of the SR-200 beryllium plates to a point load was linear prior to primary failure. Plates that were clamped on all four sides underwent three important events while responding to a concentrated point load. Primary failure was a brittle phenomenon that occurred at a load level that was approximately one-half of the ultimate load. Following ultimate failure, the specimen manifested a residual strength that was a result of delamination of the sheet material in a circular region surrounding the indentor. Clamped-free plates failed without warning in a brittle manner when undergoing an out-of-plane load.

Acknowledgments

This work was partially supported by a grant from the National Aeronautics and Space Administration, Johnson Space Center, Houston, Texas (NAG 9-280). Samples of SR-200 beryllium were provided by Brush-Wellman Corporation, Elmore, Ohio.

References

1. S.W. Tsai and E.M. Wu, *J. Compos. Mater.*, Vol 5, 1971, p 58-80
2. P. Papados and P.N. Roschke, *Proc. Int. RILEM/ESIS Conf.*, Van Nostrand Reinhold, 1991, p 673-682
3. E. Mascorro, unpublished research, Texas A&M University, 1991
4. E. Mascorro, P.N. Roschke, and P. Papados, *Proc. 9th ASCE Structures Congress*, American Society of Civil Engineers, 1991, p 362-365
5. PATRAN PLUS, Release 2.3, *User's Manual*, Vol I and II, PDA Engineering, 1988
6. R.W. Fenn, Jr., D.D. Cooks, W.C. Kinder, and B.M. Lempiere, "Test Methods for Mechanical Properties of Anisotropic Materials (Beryllium Sheet)," Technical Report AFML-TR-67-212, Lockheed Missiles and Space Company, 1967
7. S.P. Timoshenko, *Theory of Elasticity*, 2nd ed., McGraw-Hill, 1951, p 377-382
8. ABAQUS, Version 4.8, *User's Manual*, Hibbitt, Karlsson & Sorenson, 1990